Available online at www.sciencedirect.com
SCIENCE DIRECT®
Ocean Modelling 9 (2005) 31–50
Ocean Modelling
www.elsevier.com/locate/ocemod

High-frequency wind forcing of a channel model of the ACC: normal mode excitation

Wilbert Weijer *

Physical Oceanography Research Division, Scripps Institution of Oceanography, La Jolla, CA 92093-0230, USA

Received 9 March 2004; received in revised form 2 April 2004; accepted 2 April 2004
Available online 28 April 2004

Abstract

The response of the Antarctic circumpolar circulation to wind stress variability is studied in a simple model of the Southern Ocean. The model consists of a zonally reentrant channel with mid-ocean barrier, forced by surface heat flux and stochastic wind stress. The MITgcm code is used to solve for temperature, sea level, and the velocity field.

The channel transport responds actively to the stochastic wind forcing through the excitation of several eigenmodes. The fundamental basin mode is excited, which has a period of about 20 days. However, the response is dominated by a topographic mode with a period of 3 days. This barotropic mode is related primarily to topographic Rossby waves propagating on the submarine sill, and Kelvin waves propagating westward on the southern boundary. The mode shares characteristics with numerical predictions of normal modes in the Southern Ocean, as well as with recently observed modes of variability around Antarctica, with periods between 1 and 2 days. These results show that both topographic normal modes and Rossby basin modes can play a role in the adjustment of the ACC to high-frequency wind stress variability.

The presence of the resonance in the system leads to interesting phase behavior between the wind stress forcing and the ocean transport: for a considerable frequency range, the transport seems to lead the wind stress variability. This shows that the classical notion of transport passively lagging wind forcing is inadequate when eigenmodes are excited.

Keywords: Barotropic mode; Topographic waves; Oceanic response; Wind stress; Atmospheric forcing

* Tel.: +1-858-534-4274; fax: +1-858-534-9820.
E-mail address: wweijer@ucsd.edu (W. Weijer).

1463-5003/$ - see front matter
doi:10.1016/j.ocemod.2004.04.001

1. Introduction

The Antarctic Circumpolar Current (ACC) is a system of great importance for the global ocean circulation, and for the climate system as a whole. Understanding its dynamics and its sources of variability is the key for our ability to anticipate on its behavior in a changing climate. Many different mechanisms contribute to the variability in the Southern Ocean, and it is a challenge to identify the sources of specific modes of variability. This is easiest for variability in well defined frequency bands like those associated with tides and seasons (e.g., Wearn and Baker, 1980). But, for example, it is much more difficult to distinguish between a Southern Ocean response to far-field changes (Peterson and White, 1998) or a regional mode of air–sea interaction (Qiu and Jin, 1997; Weisse et al., 1999).

A good understanding of the Southern Ocean response to wind fluctuations would improve the ability to explain the observed variability. Research on the response of the Southern Ocean to fluctuating winds has focused primarily on the relation between wind stress variability and the net transport of the ACC through the Drake Passage. Many studies found coherence between wind stress fluctuations and transport, with a response time of less than two weeks (e.g., Wearn and Baker, 1980; Whitworth, 1983; Peterson, 1988; Hughes et al., 1999; Gille et al., 2001). However, the process by which this adjustment takes place is still poorly understood.

Initial adjustment of the wind-driven circulation in mid-latitude basins to time-dependent forcing is classically described in the context of barotropic planetary-waves and Rossby basin modes (e.g., Veronis and Stommel, 1956; Phillips, 1966; Willebrand et al., 1980). These modes are a sum of long-wavelength Rossby waves that satisfy the boundary conditions imposed on the boundaries of the basin. Due to their large wavelength, they transfer information across a basin within a week. Basin modes have been found in numerous modeling studies (e.g., Veronis, 1970; Willebrand et al., 1980; Barnier, 1984; Miller et al., 1987; Large et al., 1991; Pedlosky and Spall, 1999), but observational evidence is sparse. The only observation to date is usually attributed to Luther (1982), who showed evidence for basin-wide coherent oscillations in the North Pacific. But recent studies (Ponte, 1997; Hirose et al., 2001a) suggest that even this mode of variability may be a non-resonant forced response to variability in atmospheric pressure.

Most of the modeling studies cited above concentrated on flat-bottom, mid-latitude basins. But when bathymetry is taken into account, the pure basin modes are distorted, and topographically steered normal modes appear in the spectrum (e.g., Anderson et al., 1979; Willebrand et al., 1980; Barnier, 1984; Miller, 1989). There is some observational evidence for the excitation of topographic normal modes over the Iceland-Faeroe ridge (Miller et al., 1996). In addition, altimeter data from the TOPEX/Poseidon mission have revealed high levels of variability in certain basins in the Southern Ocean, where the bathymetry is characterized by the presence of closed contours of f/H (Fu et al., 2001; Webb and De Cuevas, 2002a,b, 2003; Fu, 2003). This is also suggestive of the excitation of topographic modes.

Ponte and Hirose (2004) found evidence for Kelvin waves propagating along the perimeter of Antarctica in response to fluctuations in surface pressure. They noticed an enhancement in spectral power at periods between 30 and 50 h for 3 pressure gauges situated at the perimeter of Antarctica. Based on results of a barotropic model and this pressure gauge data, they were able to identify westward propagating signals around Antarctica at 1–2 day periods. The mode they identified showed resemblance with several modes determined by Platzman et al. (1981). Platzman

et al. (1981) solved the eigenvalue problem for a global barotropic ocean model, and found several modes with a specific expression in the Southern Ocean. The slowest of these modes were related to topographic features, and could be identified as topographically trapped vorticity waves. Other modes showed characteristics of gravity waves, some with an expression around the Antarctic continent that is characteristic of the fundamental Kelvin wave. However, Platzman et al. (1981) focused on modes with periods between 8 and 80 h, and essentially excluded the frequency range of pure Rossby basin modes.

The results of Ponte and Hirose (2004) are important in the sense that they provide a glimpse of a mechanism by which the ACC could adjust to changes in atmospheric forcing. But in addition to Kelvin waves, it is possible that Rossby basin and topographic modes play a role in the adjustment process as well. In this paper results are presented which show that a combination of topographic waves, Kelvin waves and basin modes can be excited as part of the adjustment process. The research described here should be considered as a first step in studying the adjustment of the ACC to high-frequency variations in wind stress. The model that is used here pictures the Southern Ocean as a zonally reentrant channel, with a conduit and sill that represents the Drake Passage. It is shown that the model response to stochastic wind stress is dominated by a resonant mode. This mode consists of the local excitation of topographic Rossby waves on the submerged sill, and a rapid, global, adjustment of the strength of the ACC via Kelvin waves. In addition, the fundamental Rossby basin mode is excited.

2. Method

2.1. Model set-up

In this study we make use of the MITgcm code (Marshall et al., 1997a,b). The domain consists of a zonally reentrant channel with longitude λ between 0° and 90°, and latitude ϕ between 69° S and 47° S. The channel depth is 4 km. The channel is obstructed by a barrier, which is pierced by a gap of 8° wide and 2 km deep. A Gaussian bump on either side of the gap provides for a reasonably smooth transition between the abyss and the sill (Fig. 1).

Our aim is to get a first impression of the adjustment of the Southern Ocean to stochastic wind forcing, and to that end, we have chosen to keep the model as simple as possible. The Boussinesq equations are solved on a spherical grid, with 45×22 grid points in the zonal and meridional directions, respectively, yielding a horizontal resolution of $2°\times1°$. The 15 grid points in the vertical are unequally distributed, with vertical grid spacing ranging from 62 m for the uppermost layer to almost 600 m for the deepest layer.

This study will focus on the response of the ACC to zonally-averaged winds. Hence, a zonal wind stress is chosen that has a cosine profile in the meridional direction, but is zonally constant (Fig. 2a). Many studies have shown that transport fluctuations of the ACC are more coherent with zonally averaged wind stress than with local wind stress fluctuations (e.g., Wearn and Baker, 1980). This is the motivation to address this aspect first. Synoptic-scale spatial structures will be taken into account in subsequent studies.

The frictional effects of mesoscale eddies are parameterized by ordinary Laplacian friction, with vertical and horizontal viscosity coefficients A_v and A_h. No-slip boundary conditions are chosen

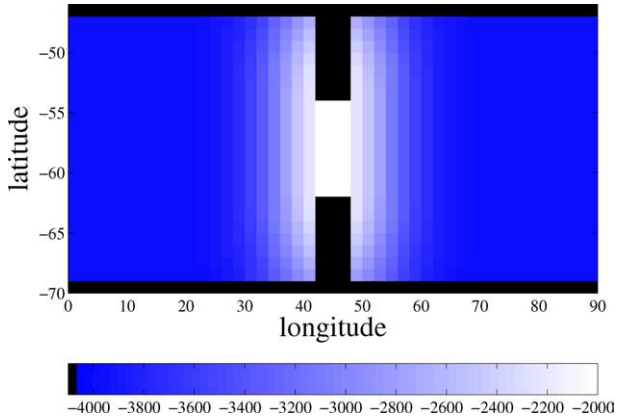

Fig. 1. Bathymetry of the zonally reentrant channel.

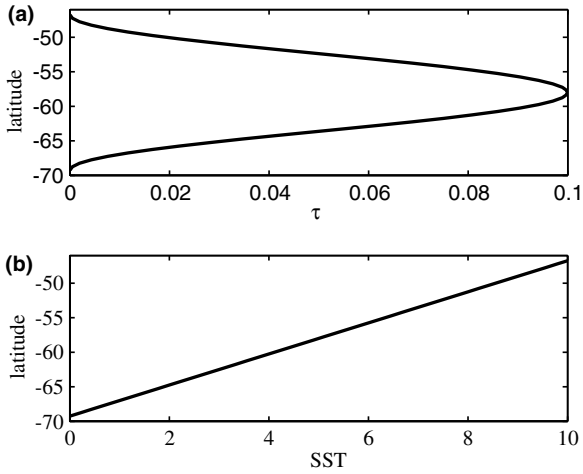

Fig. 2. Meridional profiles of (a) wind forcing (in $\mathrm{N\,m^{-2}}$) and (b) temperature forcing (°C).

for the lateral boundaries, while a quadratic friction law is applied in the bottom layer, with drag coefficient c_d.

Although transport fluctuations on seasonal and shorter time scales are dominated by barotropic fluctuations, a reasonably realistic density field is necessary to obtain an acceptable net transport. In this model density is controlled by temperature only, through a linear equation of state (with thermal expansivity α_T). Mixing is parameterized as Laplacian diffusion, with vertical and horizontal mixing coefficients κ_v and κ_h. In unstably stratified regions, vertical diffusivity is increased to κ_{ca}. In the upper layer, temperature is restored to a temperature profile that is zonally constant, but changes 10° meridionally (Fig. 2b). The relaxation time scale τ_s is set to 30 days.

Table 1
Standard values of parameters used in the calculations

Horizontal diffusivity	$\kappa_h = 1.0 \times 10^3$	$[m^2\,s^{-1}]$
Vertical diffusivity	$\kappa_v = 1.0 \times 10^{-5}$	$[m^2\,s^{-1}]$
Vertical diffusivity (unstable regions)	$\kappa_{ca} = 1.0 \times 10^2$	$[m^2\,s^{-1}]$
Horizontal viscosity	$A_h = 1.0 \times 10^5$	$[m^2\,s^{-1}]$
Vertical viscosity	$A_v = 1.0 \times 10^{-3}$	$[m^2\,s^{-1}]$
Wind stress amplitude	$\tau_0 = 0.1$	$[N\,m^{-2}]$
Thermal relaxation time scale	$\tau_s = 30$	[days]
Reference density	$\rho_0 = 1.02 \times 10^3$	$[kg\,m^{-3}]$
Thermal expansivity	$\alpha_T = 1.0 \times 10^{-4}$	$[K^{-1}]$
Bottom drag coefficient	$C_d = 0.0014$	–

The most important parameters of the model set-up are tabulated in Table 1. The most critical choice that is made is the relatively high value of the horizontal viscosity, A_h. For lower values of A_h (e.g., 10^4 $m^2\,s^{-1}$) the solution showed considerable grid-scale noise, which can be attributed to the fact that the MITgcm uses a C-grid staggering of the variables (Adcroft et al., 1999). There are ways to suppress this noise, like the C/D coupling scheme developed by Adcroft et al. (1999), or regular filtering of the variables. However, we found that either of these techniques is equivalent to adding spurious friction; it turned out that they removed crucial features of the solution field that were retained by increasing the Laplacian friction coefficient one order of magnitude. We have chosen to use the latter remedy to suppress the noise, thus retaining the basic characteristics of the solution, and being able to control and trace back the source of additional friction.

2.2. The basic steady solution

After 100 years of spin-up (with an acceleration technique applied to the temperature equation) an equilibrium was reached. Its overturning and barotropic streamfunctions are shown in Fig. 3.

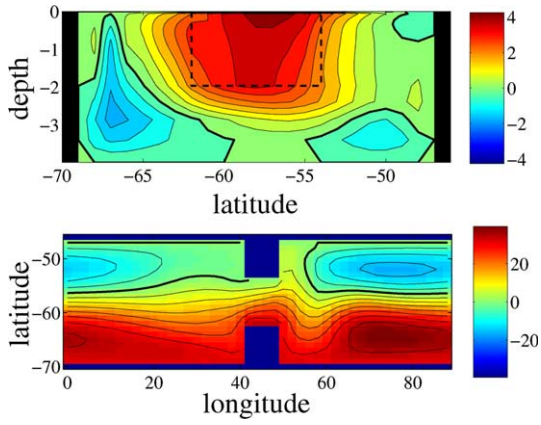

Fig. 3. Meridional overturning streamfunction (upper panel, streamlines at 0.5 Sv intervals) and barotropic streamfunctions (lower panel, streamlines at 5 Sv intervals) of the basic solution. Dashed line denotes the Drake Passage gap.

The solution shows a main overturning cell of about 4 Sv that is forced by the zonal wind stress. It consists of a northward Ekman transport and a geostrophic return flow that takes place mainly at sub-sill depths. At deeper levels a counter-clockwise circulation cell is present which is density-driven.

The barotropic streamfunction shows a 31.6 Sv transport through the Drake Passage. The main current displays a strong southward meander on the lee side of the sill. In addition, recirculation cells can be seen on either side of the main current.

When the model is forced by the density distribution and not by wind stress, a transport of only 2.3 Sv through the passage is established, whereas wind-only forces a 0.3 Sv transport. This confirms that the combination of buoyancy and wind forcing is essential to generate a strong throughflow (e.g., Borowski et al., 2002).

2.3. Stochastic forcing

Starting from the spun-up equilibrium state, a stochastic wind forcing with red spectrum is applied. This is accomplished by multiplying the zonal wind stress with a stochastic time series, $\tau_n^x(y) = \tau_0^x(y)(1 + F_n)$, with F_n constructed as outlined in Appendix A. We use 560 frequency components that are equally spaced according to: $f_i = f_0 + (i - 1)\Delta f$. With $f_0 = \Delta f = 0.0432$ cycles per day (cpd), the frequency hence ranges roughly from 0.04 to 24 cpd. The amplitudes α_i are constructed so that the amplitude spectrum of the stochastic time series displays a f^{-p} distribution, with the spectral power $-p$ taken to be -1. The standard deviation σ of the time series is taken to be 0.1. The system is integrated for roughly 910 days, yielding time series of 65,536 points.

3. Results

3.1. The Drake Passage transport

The most obvious measure of the system's variability is the net transport through the channel, and hence through the model equivalent of the Drake Passage. Fig. 4 shows that the response of the net transport clearly tends to move energy toward low-frequencies, hence reddening the spectrum. In the high-frequency range, an average spectral slope of -3 is obtained in response to the -1 slope of the forcing.

However, the most conspicuous feature in Fig. 4 is the spectral peak at a frequency of 0.3 cpd. This is caused by a resonant barotropic mode of the system, which will be discussed in the next section.

The form of the spectrum, with a resonant peak, a steep high-frequency slope and a flat low-frequency region, resembles to some extent the spectrum calculated by McWilliams et al. (1978) for their two-layer channel model with topographic blocking (TB). In their case, the forcing was constant, but eddy activity may have introduced a preferred time scale to the system. However, their peak frequency of about 1/100 cpd is far from our resonant signal. Furthermore, their sampling frequency does not resolve time scales of the oscillation found in the present model.

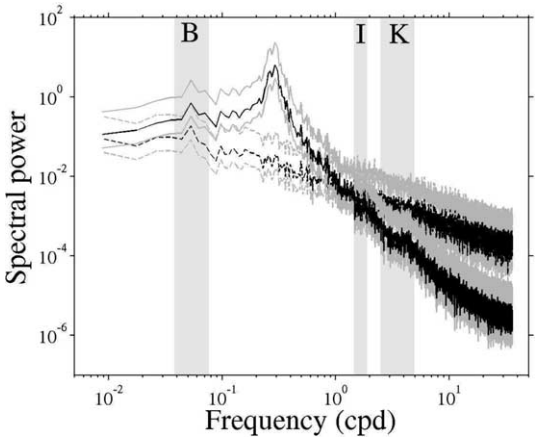

Fig. 4. Power spectra of Drake Passage transport (solid lines) and wind stress forcing (dashed lines). 95% confidence limits are denoted by the gray lines, and are calculated based on 8 subsamples of the total records. Gray areas indicate frequency bands corresponding to the fundamental basin mode ('B'), inertial oscillations ('I'), and Kelvin waves ('K').

3.2. The resonant mode

The resonant mode that is excited by the stochastic forcing completely controls the response of the transport to the wind stress fluctuations. This justifies taking a closer look at this mode.

3.2.1. Oscillatory pattern

Fig. 5 shows the evolution of sea-surface height (SSH) during one-half of an oscillatory cycle. These snapshots suggest the following mechanism: suppose there is a positive meridional gradient in sea surface height anomaly (Fig. 5, $t = \tau/8$). Consistent with the dynamics of topographic Rossby

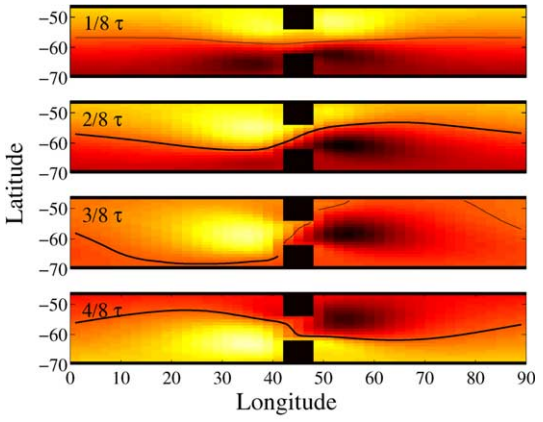

Fig. 5. Snapshots of sea-surface height, showing the evolution of the barotropic pressure field associated with the resonant mode. The 4 snapshots show the first half of an oscillatory cycle, and are 1/8th of a period apart. The run presented here is in the 'No basic' configuration (barotropic, no basic-state wind forcing; see Table 2), and is forced with a single frequency of 0.3 cpd, which surfaced as resonant frequency in the stochastically forced runs. The black line is the contour of zero anomaly.

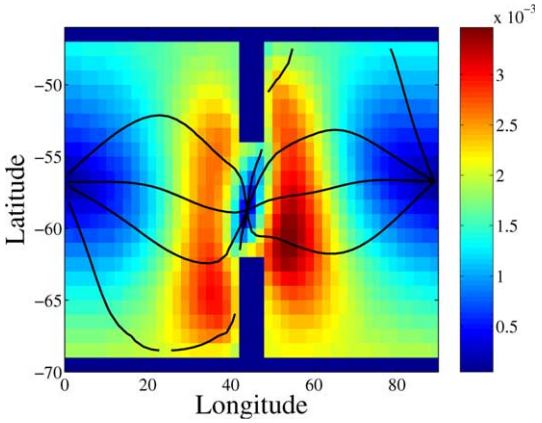

Fig. 6. Amplitude and phase lines of the oscillation in sea-surface height shown in Fig. 5. Phase lines are lines of zero amplitude. They travel clockwise through the basin and are approximately 45° apart.

waves, the positive SSH anomaly on the northern boundary starts to propagate southward on the western side of the submerged topography, while the negative anomaly in the south propagates northward on the eastern slope ($t = 2\tau/8$). These anomalies are amplified by the interaction between the sill and the anomalous eastward jet associated with the SSH gradient: obstruction of this jet by the sill causes convergence on the upstream side, thus enhancing the positive pressure anomaly. On the downstream side, divergence of the flow enhances the negative anomaly ($t = 3\tau/8$). As the anomalies continue to propagate, a negative meridional pressure gradient arises on both sides of the sill, giving rise to a westward flow anomaly over the sill ($t = 4\tau/8$). Propagation of the SSH anomalies as Kelvin waves along the southern and northern (for the positive and negative anomalies, respectively) boundaries then acts to make this anomaly circumpolar. Interaction of this negative flow anomaly with the sill sets off the second, and equivalent, half of the oscillation.

The amplitude/phase diagram of Fig. 6 gives an alternative view of the spatial and temporal characteristics of the resonant mode. SSH anomalies travel clockwise around the basin perimeter. The slow phase consists of anomalies propagating southward on the western side of the sill and northward on the eastern side. In the subsequent rapid adjustment phase, these anomalies travel as Kelvin waves, and reemerge on the opposite side of the sill.

3.2.2. Dependence on basic state

To find out which factors are important for this mode, its resonant frequency and the gain factor attained, we progressively strip off elements of the model (Table 2). Starting from the basic

Table 2
Featured runs and their characteristics

	Density forcing	Wind forcing	Bump	Free surface
Basic run	+	+	+	+
No density	−	+	+	+
No basic	−	−	+	+
No bump	−	−	−	+
Rigid lid	−	−	−	−

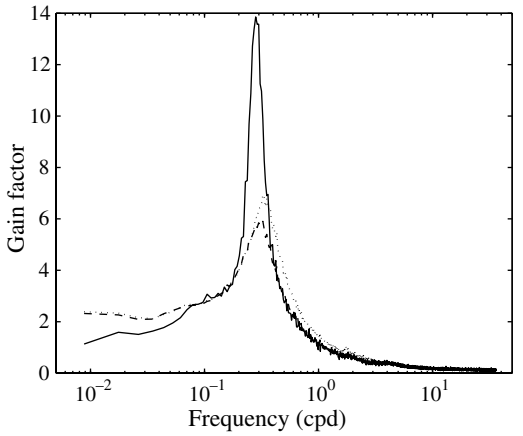

Fig. 7. Gain factor of the Drake Passage transport, defined as the square-root of the ratio of the spectra of transport and forcing time series. Spectra are averaged from 8 subsamples of complete time series. Models plotted are the 'Basic run' (solid line), 'No bump' (dashed line), and 'Rigid lid' (dotted line). Intermediate models 'No density' and 'No basic' produce curves virtually indistinguishable from the 'Basic run'. See text for explanation.

model (solid line in Fig. 7), we first remove the density equation and the density forcing ('No density'). This does not influence the resonant frequency, nor the gain factor attained. This shows that the mode is purely barotropic, and does not depend on a substantial transport through the passage.

Additionally, we remove the basic momentum forcing ('No basic'), and force the initially stagnant model with the stochastic forcing only. The same peak reappears with the same gain factor, suggesting that the mode is not influenced by the presence of the double-gyre-like background flow.

Then the Gaussian bump is removed, which was introduced to make a smooth connection between the sill and the abyss; this leaves the sill as an undersea wall. Although the gain factor is strongly reduced when this bump is removed, the resonant response is still present ('No bump'; dashed line in Fig. 7). Visual inspection of the SSH fields shows that the spatial dimensions of the anomalies on either side of the sill are much reduced; the anomaly is hence more confined to the sill, and propagates on the sill edge, rather than on the bump. The resulting motions can now be classified as so-called double Kelvin waves (Longuet-Higgins, 1968; Rhines, 1969; Mysak, 1969). These waves are equivalent to topographic Rossby waves, but travel along submarine 'escarpments' rather than slopes.

Upon changing the implicit free-surface formulation into a rigid-lid approach ('Rigid lid'), there is a slight increase in frequency and gain factor (Fig. 7, dotted line). Excursions of the sea level influence Rossby wave propagation to some extent, and generally lead to a reduction in propagation speed (Pedlosky, 1987). Thus, turning to a rigid-lid formulation might be expected to speed-up the topographic waves somewhat, and this is reflected here by the increase in resonant frequency.

Under rigid-lid conditions, Kelvin waves become infinitely fast, but since the oscillation period is limited by the propagation of the topographic waves rather than the Kelvin waves, this speed-up does not affect the overall time scale.

3.2.3. Dependence on barrier geometry

The sensitivity of the resonant mode to the shape of the submerged sill motivates testing the robustness of the mode with respect to other changes in barrier geometry.

The most significant sensitivity of both the gain factor and resonant frequency is found with respect to the sill depth (Fig. 8). Deepening of the sill strongly reduces the resonant frequency, from roughly 1 cpd for a 400 m deep sill to 0.08 cpd for a 3200 m deep sill. This tendency agrees well with the prediction for double Kelvin waves, which is, according to LeBlond and Mysak (1978):

$$\omega = f\frac{H_2 - H_1}{H_2 + H_1}. \tag{1}$$

Here, H_2 is the depth of the abyss, whereas H_1 is the depth of the sill. For sills 3600 and 4000 m deep no resonant peaks could be determined, not even after doubling the length of the time series or increasing the vertical resolution in the abyss; most of the energy is present in the lowest frequencies. For a sill deeper than 3600 m, closed f/H contours exist. This basically removes the dynamical barrier imposed by the sill.

Along with the increase in oscillation period goes an increase in resonant gain. This gain is amplified from 1.8 for a 400 m deep sill to almost 16.4 when the sill is 3200 m deep. Obviously it becomes easier for water columns to jump between the abyss and the sill when the sill becomes deeper.

There is no significant sensitivity of the resonance frequency with respect to the meridional width of the gap (Fig. 9a), or the zonal length of the sill (Fig. 9b). Only for very narrow gaps is there a tendency toward lower frequencies, accompanied by a decrease in gain. For shorter passages the gain seems to increase, while the frequency decreases. For passages of, say, 1 grid point length, the northward and southward traveling anomalies on either side of the sill interfere,

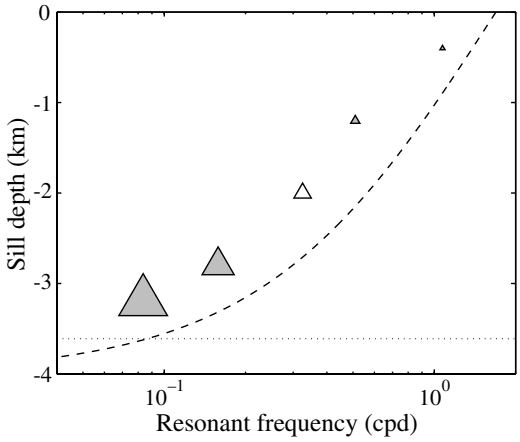

Fig. 8. Resonant frequency of the 'No bump' model, as function of sill depth. The size of the symbol is proportional to the gain factor achieved, white symbol is standard set-up. No resonant peaks could be determined for sill depths of 3.6 and 4 km. For a sill deeper than 3.6 km (dotted line), zonally connected contours of f/H exist. Black line denotes theoretical dependence of frequency on sill depth for double Kelvin waves, according to Eq. (1).

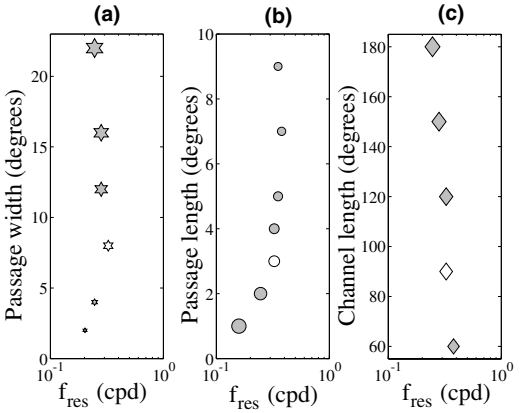

Fig. 9. As Fig. 8, but here resonant frequency as function of (a) gap (meridional) width, (b) gap (zonal) length and (c) channel length.

slowing down their propagation. This is in agreement with theory for two double Kelvin waves, trapped on either side of a ridge (Rhines, 1969).

3.2.4. Dependence on basin geometry

There is no significant impact of basin geometry on the resonance. Fig. 9c suggests a slight sensitivity of the resonant frequency with respect to the length of the basin. For rigid-lid conditions, the gain factor increases slightly from 6.3 to 8.2 while the frequency decreases from 0.37 to 0.25 cpd when changing the basin length from 60° to 180° (by tripling the number of grid points in the zonal direction). But by no means does this suggest the channel length to be a limiting factor for the oscillatory time scale.

Bringing the northern boundary northward from 47° S to 23° S, while retaining the same barrier geometry (without bump) and forcing, brings down the gain factor a bit, but does not influence the frequency. Bringing the boundary even further north to 1° N does not lead to additional reduction of the gain. This shows that the domain of influence is well south of 23° S.

Fig. 10 shows the amplitude/phase characteristics of the resonant mode in this wide basin. It displays basically the same pattern as in the normal basin in Fig. 6, with one amphidromic point above the sill and one in the basin interior. The amplitude is very small in the northern half of the basin.

These results suggest that the mode could even exist in a domain unbounded toward the north, implying that a channel geometry is not essential. From another perspective, they emphasize the importance of the interaction between the flow and the sill as an amplification mechanism of the oscillation; when the anomalies on the western side of the sill cannot be generated by incoming Kelvin waves, they must be generated locally. A description of the mode solely in terms of planetary-wave propagation is evidently not sufficient.

3.2.5. Dependence on horizontal friction

The relatively high value of eddy viscosity used in the calculations motivates an examination of the robustness of the resonance with respect to changes in horizontal mixing properties. Fig. 11

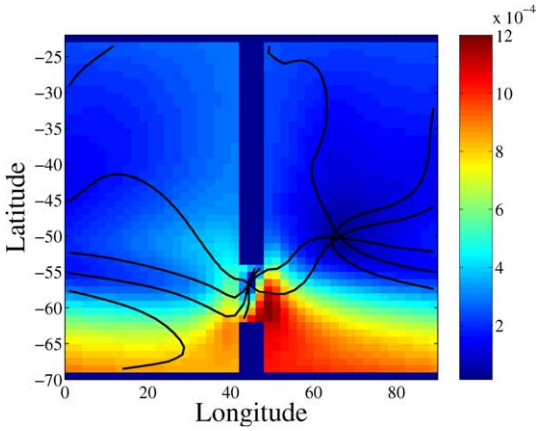

Fig. 10. As for Fig. 6, but now for the basin extending to 23° S, and with the Gaussian bump removed (but the sill retained).

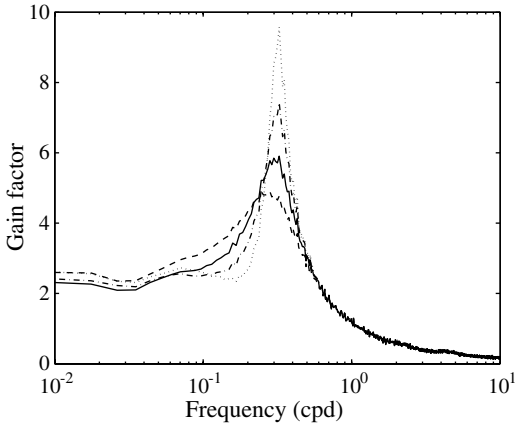

Fig. 11. Gain factor for different values of horizontal friction for the 'No bump' model. Values of κ_h plotted are 2.5 (dotted line), 5.0 (dash-dotted line), 10 (solid line), and 20 (dashed line) times 10^4 $m^2\,s^{-1}$.

shows that the gain factor of the resonance is sensitive to the value of horizontal friction, with lower friction values increasing the maximum gain while sharpening the resonant peak. The resonant frequency, however, is not significantly affected.

3.3. Basin modes

Apart from the resonant mode, the stochastic runs also feature the clear signature of a basin mode. In Fig. 12, the 3-day oscillation is clearly visible on either side of the sill, but its signal is strongly modulated by the basin mode. This mode is characterized by westward phase propa-

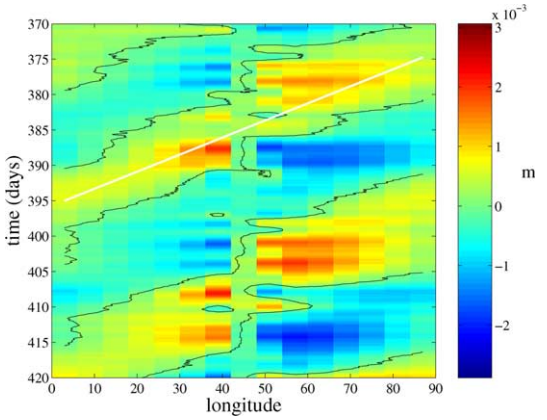

Fig. 12. Hovmüller diagram of the sea-surface height anomaly η at the central axis of the basin. Every third point in zonal direction is plotted. The 'No bump' model run is shown here (see Table 2). The white line denotes the theoretical propagation speed as given by Eq. (2).

gation, a zonal wavelength equal to the basin length, and a time scale of roughly 20 days. The phase speed of the fundamental basin mode in a basin of size $L \times W$ is given by Pedlosky (1987):

$$C = -\frac{\beta}{2\left(\frac{\pi^2}{L^2} + \frac{\pi^2}{W^2} + F\right)}, \tag{2}$$

where F is the Froude number f^2/gH. At latitude 58° S, this yields a transverse time of about 18.6 days for a basin with $L = 90°$ and $W = 22°$. The white line in Fig. 12 represents the corresponding phase velocity.

3.4. Coherence and phase between transport and wind stress

The ultimate goal of this study of Southern Ocean response to wind stress, is to better understand the part of the ocean variability that is caused by wind stress fluctuations. Fig. 13a shows the coherence between the net transport through the channel and the wind stress fluctuations. This coherence is significant for all but the highest frequencies, as can be expected from a system without any 'noise' due to, e.g., mesoscale variability, tides, etc. The largest coherence is found for the lowest frequencies.

However, the most interesting aspect of the coherence is the phase angle between wind stress and transport fluctuations, and the corresponding time lag; starting from the highest frequencies, the phase angle decreases from 0° toward −90° (Fig. 13b). This results in a maximum time lag of 0.6 days for a forcing period of 3 days, with the wind stress leading the transport. However, at the resonant frequency, the phase angle changes sign, so that for lower frequencies the transport seems to lead the wind stress by about 30° (or, equivalently, a phase lag of 330°). This corresponds to a time lead of up to a week.

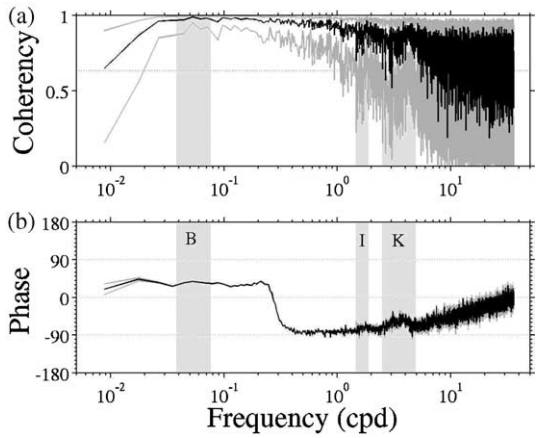

Fig. 13. (a) (Squared) coherence and (b) phase between Drake Passage transport and wind stress. In (b), negative phase means that transport lags wind.

4. Discussion

In this simple model, the ACC responds coherently to wind stress fluctuations. However, it does not respond *passively* to the variability of the wind stress forcing; instead, the ACC reacts through the excitation of eigenmodes. This has interesting consequences for the phase relation between transport variability and wind stress fluctuations: in particular the excitation of the topographic Rossby mode results in the transport variability seemingly *leading* the wind stress for a large region in the frequency domain. Obviously, the classical notion of a 'lag' between transport and wind stress, as advocated by, e.g., Wearn and Baker (1980), loses its meaning when resonant modes come into play.

Phase shift across a resonance is typical behavior for resonant systems. There are a couple of systems in oceanography where such a phase inversion seems to occur. A well known example is the excitation of tidal resonances in semi-enclosed basins. Webb (1973), for instance, studied tidal resonance in the Coral Sea, and found a negative phase lag for a substantial area in the equatorial Pacific. Another resonant system is the excitation of inertial motions in the wind-forced Ekman layer. As shown by Gonella (1972), a phase inversion occurs at the inertial frequency when the Ekman layer is forced by a rotating wind. The requirement for a resonant mode to invert the phase relationship is obviously that the resonant response is strong enough to dominate all other variability related to wind stress fluctuations. The mode hence must be able to pick up enough energy from the wind stress to sustain a considerable-amplitude signal against friction. In this model, with all its simplicities, this is obviously the case. Ponte and Hirose (2004) show that the Southern Ocean mode in their model is only weakly forced and strongly damped, and their data suggest even stronger damping in the real ocean. Therefore, whether all the complicating factors in the real Southern Ocean allow for such large-amplitude response remains a problem to be addressed with more realistic models, and a thorough analysis of available data.

Two distinct modes of adjustment were identified in this model. We found evidence for the excitation of the fundamental basin mode, which has a time scale of about 20 days. But the

strongest response was due to the resonant excitation of a topographic mode. With its 3-day period, it consistently dominated the time series of the channel transport. In fact, this mode displays strong similarities with normal modes that have been found in the Southern Ocean. The modes described by Ponte and Hirose (2004) consist of a strong, trapped wave propagating westward around Antarctica, and a weaker amphidromic system in the Pacific, Atlantic and Indian Ocean basins. In this respect they resemble mostly the mode that was numbered 16 by Platzman et al. (1981). The westward propagation along the southern model boundary is an important element of the oscillation in our model.

In this model, however, the wave clearly arises from interaction of the flow with a submerged sill. This accounts for the difference in time scale between our mode and the Kelvin mode of Ponte and Hirose (2004). None of the vorticity modes identified by Platzman et al. (1981) were explicitly related to bathymetric features within the Drake Passage itself, but some of the modes show enhanced energy there (for instance, the 'Falkland Plateau mode' 1, the 'Patagonian Shelf modes' 7 and 8, and the 'Kerguelen mode' 13). The barrier that is included in this model is much simpler than the bathymetry that blocks the ACC; the main barrier obstructing the circumpolar flow is the narrow Scotia Ridge, which is shallower than 2000 m at most places. The complexity of this bathymetry, and its relatively small spatial scales, make it difficult to resolve in numerical models as used by Platzman et al. (1981). Indeed, Hirose et al. (2001b) showed a considerable improvement in the response variance of a barotropic ocean model to atmospheric forcing when changing from smoothed to unsmoothed 1.125° bathymetry. So, the absence of a topographic mode within the Drake Passage in the analysis of Platzman et al. (1981) does not exclude the possibility that the actual bathymetry could support topographic modes. A pressure gauge array along the Scotia Ridge should be able to detect propagating signals associated with topographic Rossby waves.

Basin modes are consistently found here, for all basin geometries applied. Their frequencies correspond well to theoretical estimates. The 20-day oscillation period of the Rossby basin mode in this study is mainly determined by geometric considerations (Eq. (2)), and these are obviously not realistically represented in this channel model. Theoretically, a minimum period of 7.5 days (at 58° S) can be achieved when the spatial scales of the basin are so large that the denominator in Eq. (2) is dominated by the Froude number F. A 8.6-days period is found for the domain that extends to the equator.

However, the role of basin modes in the adjustment of the real Southern Ocean remains a topic of further study; their presence, stability and spatial patterns can be strongly modified by complex bathymetry (Miller, 1989), and, as mentioned before, this bathymetry is not well represented here. The fact that the Southern Ocean is largely unbounded toward the north may be a reason for concern with respect to the existence of basin modes. However, our results for a domain extending to the equator show a clear basin mode signature. And being geostrophically balanced features, it is unlikely that basin modes extend across the equator.

Another reassuring feature is the fact that the basin mode seems to be unharmed by the presence of the Drake Passage gap in this model. Basin modes exist as a result of the reflection of Rossby waves on basin boundaries, and it is not clear a priori whether the Drake Passage gap acts as a boundary for long planetary-waves. The width of the Drake Passage is approximately 700 km (890 km in this model), which is smaller than the roughly 2000 km Rossby radius of deformation, or the 1000 km of characteristic storm systems. Pedlosky (2001) showed that a barrier pierced by

two or more narrow passages could be very effective in the transmission of Rossby waves, but a single narrow gap, such as the Drake Passage, allows for little energy transfer. So obviously, the Drake Passage acts as a barrier to Rossby waves and is able to reflect their energy; this paves the road for local interference between incoming and reflected waves, allowing for the existence of basin modes.

All in all, this study has given us a first impression of the possible modes of response of the Southern Ocean to wind variability. Following steps are to study the impact of realistic bathymetry on the adjustment process, and the response to localized winds with realistic and variable spatial structures.

5. Summary and conclusion

This study addresses the problem of how a flow in a zonally reentrant channel, obstructed by a mid-ocean sill and barrier, responds to high-frequency stochastic wind forcing. This response is found to be controlled by several fundamental modes of adjustment, in particular the fundamental basin mode and a topographic normal mode. The latter consists of topographic waves propagating along the submerged sill, followed by rapid adjustment through Kelvin waves. It is argued that this mode shows similarities with normal modes calculated by Platzman et al. (1981), and with a mode of variability recently observed in the Southern Ocean by Ponte and Hirose (2004).

The excitation of this mode leads to rather complicated phase behavior between the net zonal transport and the wind stress. For frequencies higher than the resonant frequency of about 3 days, the transport lags the wind stress. However, the phase changes sign at the resonant frequency, so that for lower frequencies the transport variations seem to *lead* wind stress fluctuations. Hence, the classical notion of a 'lag' between transport and wind stress loses its significance when resonant modes are excited.

Acknowledgements

Ongoing support from Sarah Gille is gratefully acknowledged. Two anonymous reviewers are thanked for their constructive comments. This research was supported by the NASA Ocean Vector Wind Science Team, JPL contract 1222984.

Appendix A. Stochastic time series with red spectrum

A time series F^n is constructed that has a red ($\propto f^{-p}$) spectrum. It consists of a summation of N oscillations, with random phases and frequency-dependent amplitudes. For every time t^n, the following sum is evaluated:

$$F^n = F_0 \sum_{i=1}^{N} \alpha_i \cos(2\pi f_i t_n + \phi_i^n) \tag{A.1}$$

with

$$\alpha_i = \frac{\alpha_0}{\sqrt{N f_i^p}}. \tag{A.2}$$

The phase ϕ_i^n is a random number $\in [0, 2\pi]$; its time-dependence is determined later. If the frequency components are considered as independent (which is not completely true due to the time-dependent phases), the variance of this series is given by

$$\sigma^2 = \frac{F_0^2}{2} \sum_{i=1}^{N} \alpha_i^2 = F_0^2 \frac{\alpha_0^2}{2N} \sum_{i=1}^{N} \frac{1}{f_i^p} \tag{A.3}$$

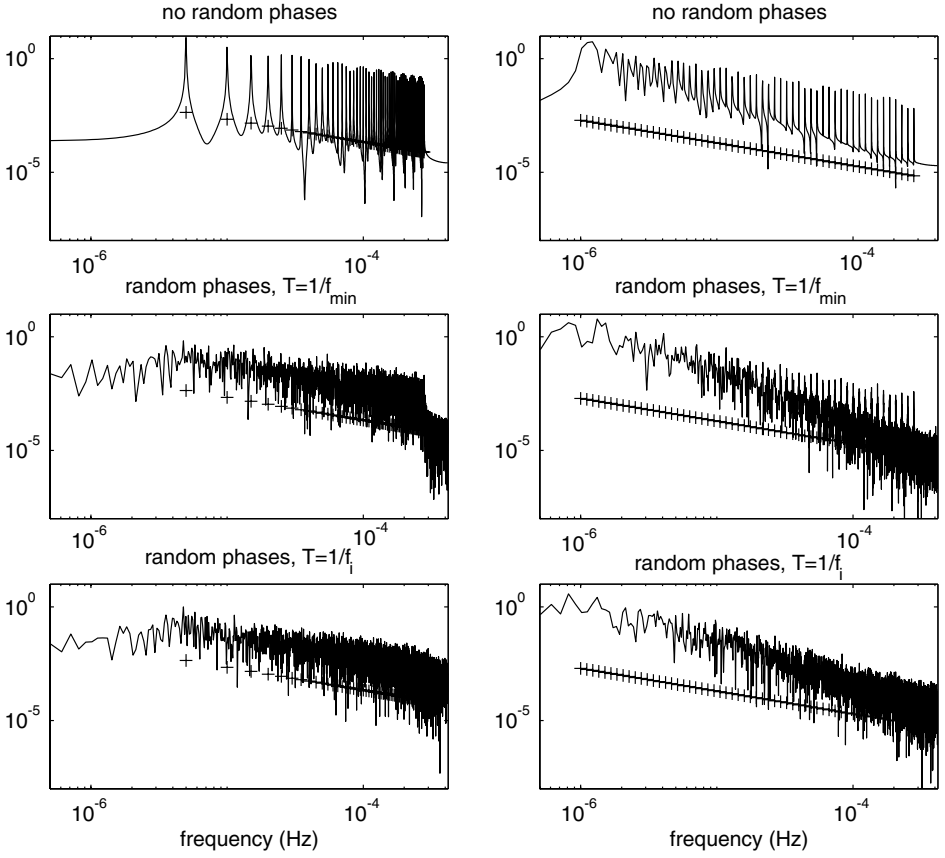

Fig. 14. Spectra of several time series showing the impact of the random-phases algorithm. The time series consist of 8192 time steps of 1200 s, and are constructed using 56 frequency components with amplitudes determined by Eq. (A.2) and $p = 1$. For the left column, these frequency components are equally spaced, whereas for the right column they are logarithmically distributed. For the upper panels no phases are assigned to the modes, giving rise to sharp peaks for the specific frequency components. For the central panels, random phases are applied, but the phase step $\Delta\varepsilon$ is the same for all components and based on the smallest frequency; the highest frequencies still show the spiky behavior. For the lower panels the phase shift is frequency-dependent according to Eq. (A.7). Note that the logarithmic distribution of f leads to a slight additional reddening of the spectrum.

can now be adjusted to normalize the series, so that $\sigma = F_0$:

$$\alpha_0 = \sqrt{\frac{2N}{\sum_i \frac{1}{f_i^p}}}. \tag{A.4}$$

The time series thus constructed has a cycle length of $T = 1/\min(f)$. To avoid repetition of the cycle when the integration is extended, the phases ϕ_i are made time-dependent through a stochastic process:

$$\phi_i^n = \phi_i^{n-1} + \varepsilon_i^n, \tag{A.5}$$

where $\varepsilon_i^n = \zeta^n \Delta\varepsilon_i$, and ζ is taken from a uniform distribution $\mathscr{U}(-1, 1)$. The standard deviation for such a process is given by

$$\sigma_{n,i}^2 = \frac{1}{3} n \Delta\varepsilon_i^2. \tag{A.6}$$

We want to allow the phase of a frequency component to change between roughly $[-\pi, \pi]$ during an oscillation period $1/f_i$, so

$$\Delta\varepsilon_i = \pi\sqrt{(3\Delta t f_i)}, \tag{A.7}$$

where Δt is the actual time step of the integration. Due to the frequency- and time-dependent phases, the frequency components are not completely independent, so the amplitude equation (A.2) does not guarantee a perfect f^{-p} dependency of the power spectrum (Fig. 14).

References

Adcroft, A., Hill, C., Marshall, J., 1999. A new treatment of the Coriolis terms in C-grid models at both high and low resolutions. Mon. Weather Rev. 127, 1928–1936.

Anderson, D.L.T., Bryan, K., Gill, A.E., Pacanowski, R.C., 1979. The transient response of the North Atlantic: some model studies. J. Geophys. Res. 84, 4795–4815.

Barnier, B., 1984. Influence of a mid-ocean ridge on wind-driven barotropic Rossby waves. J. Phys. Oceanogr. 14, 1930–1936.

Borowski, D., Gerdes, R., Olbers, D., 2002. Thermohaline and wind forcing of a circumpolar channel with blocked geostrophic contours. J. Phys. Oceanogr. 32, 2520–2540.

Fu, L.-L., 2003. Wind-forced intraseasonal sea level variability of the extra-tropical oceans. J. Phys. Oceanogr. 33, 436–449.

Fu, L.-L., Cheng, B., Qiu, B., 2001. 25-Day period large-scale oscillations in the Argentine Basin revealed by the TOPEX/Poseidon altimeter. J. Phys. Oceanogr. 31, 506–517.

Gille, S.T., Stevens, D.P., Tokmakian, R.T., Heywood, K.J., 2001. Antarctic Circumpolar Current response to zonally averaged winds. J. Geophys. Res. 106, 2743–2759.

Gonella, J., 1972. A rotary-component method for analysing meteorological and oceanographic vector time series. Deep-Sea Res. 19, 833–846.

Hirose, N., Fukumori, I., Ponte, R.M., 2001a. A non-isostatic global sea level response to barometric pressure near 5 days. Geophys. Res. Lett. 28, 2441–2444.

Hirose, N., Fukumori, I., Zlotnicki, V., 2001b. Modeling the high-frequency barotropic response of the ocean to atmospheric disturbances: sensitivity to forcing, topography, and friction. J. Geophys. Res. 106, 30987–30995.

Hughes, C.W., Meredith, M.P., Heywood, K.J., 1999. Wind-driven transport fluctuations through Drake Passage: a southern mode. J. Phys. Oceanogr. 29, 1971–1992.

Large, W.G., Holland, W.R., Evans, J.C., 1991. Quasi-geostrophic ocean response to real wind forcing: the effects of temporal smoothing. J. Phys. Oceanogr. 21, 998–1017.

LeBlond, P.H., Mysak, L.A., 1978. Waves in the ocean. In: Elsevier Oceanography Series, vol. 20. Elsevier, Amsterdam. 602 pp.

Longuet-Higgins, M.S., 1968. On the trapping of waves along a discontinuity of depth in a rotating ocean. J. Fluid Mech. 31, 417–434.

Luther, D.S., 1982. Evidence of a 4–6 day barotropic, planetary oscillation of the Pacific Ocean. J. Phys. Oceanogr. 12, 644–657.

Marshall, J., Adcroft, A., Hill, C., Perelman, L., Heisey, C., 1997a. A finite-volume, incompressible Navier–Stokes model for studies of the ocean on parallel computers. J. Geophys. Res. 102, 5753–5766.

Marshall, J., Hill, C., Perelman, L., Adcroft, A., 1997b. Hydrostatic, quasi-hydrostatic, and non-hydrostatic ocean modelling. J. Geophys. Res. 102, 5733–5752.

McWilliams, J.C., Holland, W.R., Chow, J.H.S., 1978. A description of numerical Antarctic Circumpolar Currents. Dyn. Atmos. Oceans 2, 213–291.

Miller, A.J., 1989. On the barotropic planetary oscillations of the Pacific. J. Mar. Res. 47, 569–594.

Miller, A.J., Holland, W.R., Hendershott, M.C., 1987. Open-ocean response and normal mode excitation in an eddy-resolving general circulation model. Geophys. Astrophys. Fluid Dyn. 37, 253–278.

Miller, A.J., Lermusiaux, P.F.J., Poulain, P.-M., 1996. A topographic-Rossby mode resonance over the Iceland-Faeroe ridge. J. Phys. Oceanogr. 26, 2735–2747.

Mysak, L., 1969. On the generation of double Kelvin waves. J. Fluid Mech. 37, 417–434.

Pedlosky, J., 1987. Geophysical Fluid Dynamics. Springer-Verlag, New York, USA. 710 pp.

Pedlosky, J., 2001. The transparency of ocean barriers to Rossby waves: the Rossby slit problem. J. Phys. Oceanogr. 31, 336–352.

Pedlosky, J., Spall, M., 1999. Rossby normal modes in basins with barriers. J. Phys. Oceanogr. 29, 2332–2349.

Peterson, R.G., 1988. On the transport of the Antarctic Circumpolar Current through Drake Passage and its relation to wind. J. Geophys. Res. 93, 13993–14004.

Peterson, R.G., White, W.B., 1998. Slow oceanic teleconnections linking the Antarctic Circumpolar Wave with the tropical El Niño—Southern Oscillation. J. Geophys. Res. 103, 24573–24583.

Phillips, N.A., 1966. Large-scale eddy motion in the western Atlantic. J. Geophys. Res. 71, 3883–3891.

Platzman, G.W., Curtis, G.A., Hansen, K.S., Slater, R.D., 1981. Normal modes of the World Ocean. Part II: description of modes in the period range 8 to 80 hours. J. Phys. Oceanogr. 11, 579–603.

Ponte, R.M., 1997. Nonequilibrium response of the global ocean to the 5-day Rossby–Haurwitz wave in atmospheric surface pressure. J. Phys. Oceanogr. 27, 2158–2168.

Ponte, R.M., Hirose, N., 2004. Propagating bottom pressure signals around Antarctica at 1–2 day periods and implications for ocean modes. J. Phys. Oceanogr. 34, 284–292.

Qiu, B., Jin, F.-F., 1997. Antarctic Cirumpolar Waves: an indication of ocean-atmosphere coupling in the extratropics. Geophys. Res. Lett. 24, 2585–2588.

Rhines, P.B., 1969. Slow oscillations in an ocean of varying depth. Part I: abrupt topography. J. Fluid Mech. 37, 161–189.

Veronis, G., 1970. Effect of fluctuating winds on ocean circulation. Deep-Sea Res. 17, 421–434.

Veronis, G., Stommel, H., 1956. The action of variable wind stresses on a stratified ocean. J. Mar. Res. 15, 43–75.

Wearn, R.B., Baker, D.J., 1980. Bottom pressure measurements across the Antarctic Circumpolar Current and their relation to the wind. Deep-Sea Res. 27A, 875–888.

Webb, D.J., 1973. Tidal resonance in the Coral Sea. Nature 243, 511.

Webb, D.J., De Cuevas, B.A., 2002a. An ocean resonance in the Indian sector of the Southern Ocean. Geophys. Res. Lett. 29 (14), 10.1029/GL015270.

Webb, D.J., De Cuevas, B.A., 2002b. An ocean resonance in the Southeast Pacific. Geophys. Res. Lett. 29 (8), 10.1029/2001GL014259.

Webb, D.J., De Cuevas, B.A., 2003. The region of large sea surface height variability in the southeast Pacific Ocean. J. Phys. Oceanogr. 33, 1044–1056.

Weisse, R., Mikolajewicz, U., Sterl, A., Drijfhout, S.S., 1999. Stochastically forced variability in the Antarctic Circumpolar Current. J. Geophys. Res. 104, 11049–11064.

Whitworth, T., 1983. Monitoring the transport of the Antarctic Cirumpolar Current at Drake Passage. J. Phys. Oceanogr. 13, 2045–2057.

Willebrand, J., Philander, S.G.H., Pacanowski, R.C., 1980. The oceanic response to large-scale atmospheric disturbances. J. Phys. Oceanogr. 10, 411–429.